Nanometrical Helical Structures as Platform to Induce Chiroptical Properties to Achiral Components

Reiko Oda, Thierry Buffeteau, Yutaka Okazaki, Yann Battie, Emilie Pouget, Sylvain Nlate, Naoya Ryu, Dario M. Bassani

“keywords/abstract

Dear Author,

Keywords and abstracts will normally not be included in the print version of your chapter but only in the online version (if not decided differently by Wiley-VCH).

Thank you!”

Abstract

Keywords

Author Queries

AQ1	Please provide street name in affiliation 3 and 5.
AQ2	We have shortened running head of Chapter Title, as it exceeds the hsize value. Please check and confirm, is this fine?
AQ3	Kindly provide opening bracket.

8

Nanometrical Helical Structures as Platform to Induce Chiroptical Properties to Achiral Components

Reiko Oda[1,2], Thierry Buffeteau[3], Yutaka Okazaki[1,4], Yann Battie[5], Emilie Pouget[1], Sylvain Nlate[1], Naoya Ryu[6], and Dario Bassani[3]

[1]CNRS – Universite Bordeaux – Bordeux INP, Institute of Chemistry and Biology of Membranesl and Nanoobjects (UMR5248 CBMN), 2 rue Robert Escarpit, 33607 Pessac, France
[2]Tohoku University, WPI-Advanced Institute for Materials Research, Katahira, Aoba-Ku, 980-8577 Sendai, Japan
AQ1 *[3]CNRS, University of Bordeaux, Institut des Sciences Moléculaires, (UMR5255 ISM), 33405 Talence, France*
[4]Kyoto University, Graduate School of Energy Science, Yoshida-Honmachi, Sakyo-ku, 606-8501 Kyoto, Japan
[5]Université de Lorraine, Laboratoire de Chimie et Physique – Approach Multi-échelles des milieux, (LCP-A2MC), 57078 Metz, France
[6]Kumamoto Industrial Research Institute 3-11-38 Higashimachi, Materials Development Department, Higashi-ku, Kumamoto 862-0901, Japan

8.1 Introduction

Chirality is amongst the few properties of matter that manifest themselves ubiquitously from large macroscopic objects to subatomic particles. The two enantiomers of a chiral structure (material or molecule) have almost the same properties as individual species, but the differences become pronounced when they interact with other chiral structures or an external field (enantioselectivity). The chiroptical properties of chiral molecules due to inherent molecular asymmetry factors are limited by our ability to synthesize large molecules. The large majority of chiral molecules have dissymmetry g-factor ($\Delta\varepsilon/\varepsilon$) lower than 10^{-3} [1]. Promising approaches to enhance the chiroptical signals include hierarchical or mesoscopic luminophores such as intramolecular self-assemblies [2], liquid crystal, or polymers [3–5] with strong cooperative effect (chiral amplification). The concept of the transmission of chirality information, generally called chirality transfer or chirality induction, is an interesting approach that can be observed at different levels. In the large majority of the cases, they are observed between a part of a molecule and another part of the same molecule (intra-molecular) or from a chiral (supra)molecule to another (supra)molecule (inter-(supra)molecular). Where the transmission of the chiral information is observed between the entities of similar sizes, an interesting extension that gives access to the transmission of chiral information spanning over different scales and functions can be observed in the cases where chiral molecule self-assembles to form nanometric or micrometric chiral structures (chirality amplification) and inversely from a chiral mesoscopic structure or a patterned

Chiral Luminescence: From Molecules to Materials and Devices, First Edition. Edited by Kazuo Akagi.

surface to achiral molecule or nanoparticles. Among various mesoscopic structures, nanoparticles of 1–100 nm have been used in a wide range of fields, because they exhibit unique physical/optical properties different from solid bulk materials due to the quantum size effect. The combination of chiral nanoparticles and chiral molecules based on the strong interaction between plasmonic states of chiral nanomaterials with circularly polarized photons [6–11] has therefore promising potential as molecular markers and enantioselective detections [12, 13]. There have been reports on asymmetric interactions between chiral gold nanoparticles (GNPs) with chiral molecules and biomolecules [14, 15]. Such strong circularly polarized signals show promising applications in the biomedical field as biomarkers to detect neurodegenerative diseases [16].

We have developed unique supramolecular double template method using a soft template with shape-controllable nano morphology to fabricate hard, helical silica outer shells containing nanometric morphological information on chiral objects (pitch and handedness) on the order of tens to hundreds of nanometers. By densely organizing molecules and particles on its surface, it is possible to transfer chiral properties to the long-range aggregates of achiral molecules and particles [17]. This method allows us to design new chiral materials in which chiral information from nano/macroscopic platforms onto small molecules and nanoparticles resulting in chiroptical signals on achiral entities defined as induced circular dichroism (ICD) or induced circularly polarized luminescence (ICPL) [18, 19].

In this chapter, we will present the ensemble of examples we have demonstrated in which a small chiral molecule is used to design nanometric chiral platforms with a few hundred nanometer, which then were used as a matrix for the amplification of chirality of a variety of chromophores in order to design functional nanostructures.

8.2 Molecular and Supramolecular Chirality from Gemini-Tartrate Templates

8.2.1 Gemini-tartrate Amphiphiles – Formation of Gels with Chiral Nanoribbon Structures

The helical supramolecular nanoplatform is prepared as previously reported method using achiral cationic gemini surfactants having the formula C_2H_4-1,2-$((CH_3)_2N^+C_{16}H_{33})_2$, denoted as gemini or 16-2-16 hereafter in the presence of chiral tartrate. In water they form nanometrical twisted or helical ribbons as well as tubules as observed by transmission electron microscope (TEM) (Figure 8.1) [20, 21]. The handedness of the helices depends on the D- or L-chiral configuration of tartrate (Right-handed ribbons are formed in the presence of L-tartrate and left-handed ribbons are formed with D-tartrate.). The pitch and width of these helices decrease continuously upon increasing the enantiomeric excess (ee), from flat multilayer membranes for the racemate (infinite pitch) to the twisted ribbons (with Gaussian curvature, Figure 8.1a) with 100 nm pitch, and to the helical ribbons (cylindrical curvature, Figure 8.1b) with about 65 nm pitch, and the tubules (Figure 8.1c) for the pure enantiomer [22].

Color Fig: **8.1**

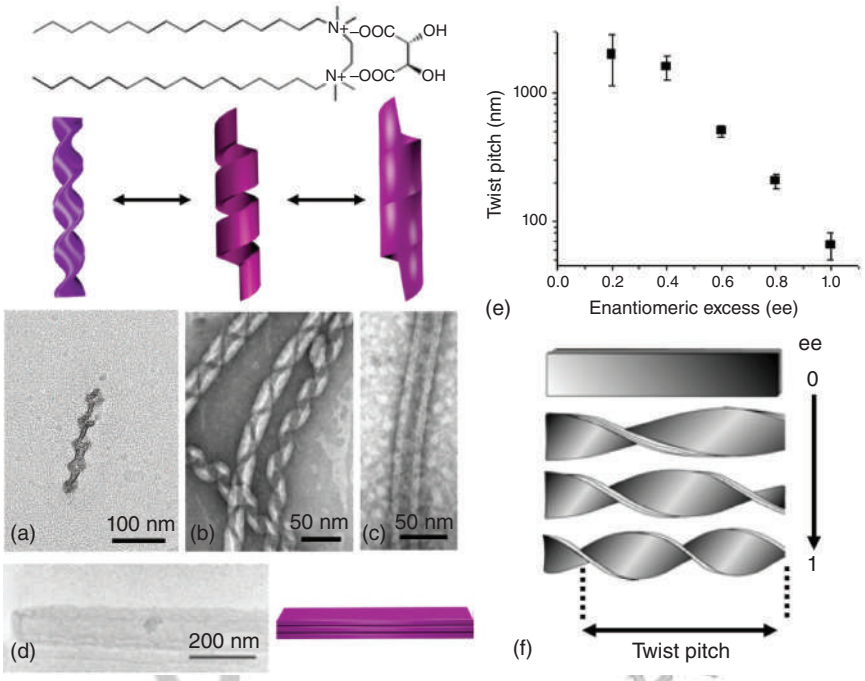

Figure 8.1 Chemical structure of 16-2-16 L-tartrate. Transmission electron microscopy (TEM) images and schematic representations of a twisted ribbon (a), a helical ribbon (b), and a tubule (c) and a flat ribbon of racemic 16-2-16 tartrate (d). The morphologies of the multilayer ribbons depend on the ee of the tartrate counterion. For a pure enantiomer, twisted ribbons form first, and transform into helical ribbons and tubules with time. This transformation into helical ribbons or tubules subsists at an ee as low as 0.8, but only twisted ribbons are observed below ee = 0.6. The pitch of the twist increases with decreasing ee (e and f) up to an infinite value for ee = 0 (flat ribbon). Source: Reproduced with permission from John Wiley & Sons, Inc., 2018.

Detailed study by small-angle and wide-angle X-ray scattering (SAXS and WAXS) associated with molecular modeling revealed that the ribbons formed with 16-2-16 tartrate follow well-defined and crystalline molecular organization [23]. They are made of stacked heterochiral bilayers comprised of homochiral monolayers, and this organization is conserved through large morphology transitions from racemic (i.e. flat multilayered ribbons) to helical ribbons or tubules for the pure enantiomer. The chirality of mono/bilayers are defined not only by the molecular chirality of tartrate (D- or L-) but through the propagation of hydrogen bonds between tartrates and crystalline water molecules, and by the dications that are intrinsically achiral but adopt two mirror-image conformations of their headgroups, i.e. through the formation of strong ion pair with dianion tartrate. The contact domain between adjacent bilayers is homochiral: both gemini headgroups and tartrate of the symmetrical leaflet have the same chirality.

Along with detailed circular dichroism (CD) studies reported previously [24, 25], the XRD analysis described above gives us a global view on this simple but beautiful

system. Chiral counterions and nonchiral gemini surfactants form crystalline bilayers with well-defined chiral organization with a long-range hydrogen-bonded network, leading to the formation of chiral ribbons. Thus chiral information is transmitted from tartrate to gemini molecules, which leads to the chiral assemblies (with chiral conformation) expressing the chirality at mesoscopic level.

8.2.2 Organic–Inorganic Nanohelices

The structural diversity of the nanometric chiral nanoribbons based on the self-assembled gemini-tartrate as described above inspired us to exploit them as templates for inorganic chiral nanostructures fabrication with controlled pitch and handedness by sol–gel reaction of tetraethoxysilane (TEOS) [26, 27]. After transcription, calcination was performed by heating the silica–amphiphilic molecules hybrid nanoribbons at 600°C for two hours under air (Figure 8.2a). After the calcination process, both twisted and helical morphologies were maintained (Figures 8.2b,c, right), but they shrank in all the three dimensions (thickness of silica wall, pitch, and width of the ribbons as defined in Figure 8.2d) by about 16–17% [28, 29].

8.2.3 Chirality of Siloxane Network of the Silica Nanohelices

If the chiral shape of the helical and twisted silica nanoribbons is evident from the TEM observations, the chirality at the interatomic level inside the silica walls is not obvious. Infrared (IR) measurements of these silica nanoribbons exhibit specific vibrational signals of silica in the 900–1250 cm^{-1} spectral range [28]. The band located at 1090 cm^{-1} and its shoulder at 1240 cm^{-1} are associated with the transverse optic (TO) and longitudinal optic (LO) modes of the Si–O–Si asymmetric stretching vibration (ν_aSi–O–Si), respectively. The band at 960 cm^{-1} is assigned to the Si–OH stretching vibration of free silanol groups. Surprisingly, vibrational CD (VCD) measurements clearly demonstrated Cotton effect both for the LO and TO modes. The VCD spectra of L-silica–gemini hybrid twisted nanoribbons (L-tw) presented a strong negative–positive (from long to short wavenumbers) Cotton effect for the TO mode at 1090 cm^{-1} and a much weaker negative Cotton effect for the LO mode. Opposite spectra were obtained for D-silica-gemini hybrid twisted nanoribbons (D-tw). The two components of the 1090 cm^{-1} band are probably due to the coupling of the different ν_aSi–O–Si vibrators, which are distributed in a chiral arrangement within the silica network. Similar phenomenon was observed with the $\nu_a CH_2$ vibration of 16-2-16 alkyl chains confined in the organic–inorganic hybrid helices. These results unambiguously indicate that chiral information on organic template was transcribed to the silica nanoribbons. Although a few VCD spectra of siloxane-based materials have been reported in the literature for ladder-like silsesquioxane polymers [30] and for micrometric chiral mesoporous silica particles [31], no such strong VCD signals of silica chiral nanostructures with clear opposite signals for two enantiomers have been reported before, which enable quantitative evaluation of the chiral information on silica nanoribbons. After the calcination at

Color Fig: **8.2**

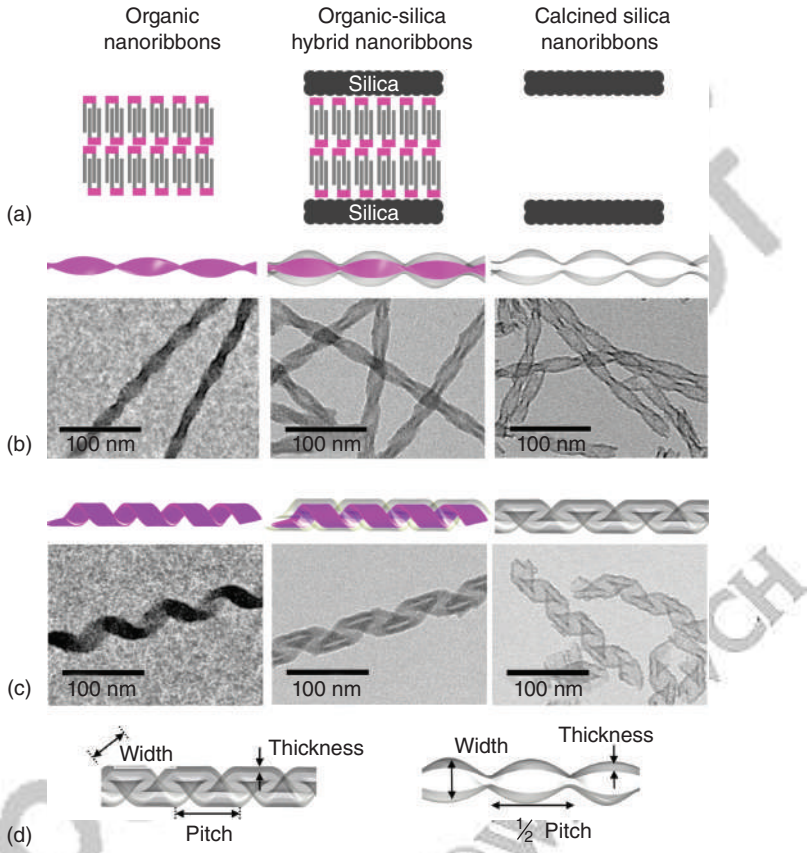

Figure 8.2 (a) Schematic illustrations of cross-sectional surfaces of nanoribbons (left), silica–gemini hybrid nanoribbons before (middle) and after (right) calcination. TEM images of twisted (b) nanoribbons prepared by one hour aging or helical (c) nanoribbons after three days aging of 16-2-16 L-tartrate (1 mM) aqueous solution at 20°C (left). The same samples after sol–gel reaction of TEOS (middle) and after calcination at 600°C for two hours (right). Source: Reproduced with permission from John Wiley & Sons, Inc., 2018.

600 °C, the intensity of the Si–OH stretching band at 960 cm^{-1} reduced in agreement with the Si–O–Si bond formation (silanol condensation reaction) during calcination. An important increase in VCD signal for the bands at 1100 and 1240 cm^{-1} was observed upon calcination, and the dimensionless dissymmetric factor $g = \Delta A/A$ of calcinated silica twisted or helical nanoribbons ($g_{tw\text{-}calc}$ or $g_{hel\text{-}calc}$) is about 1.7 or 1.9 times larger than that of uncalcinated silica–gemini hybrid twisted or helical nanoribbons (g_{tw} or g_{hel}), respectively. This is likely related to the global shrinkage of nanoribbons and stronger silica network constraint after calcination as described above. Therefore, chirality probably originates from the siloxane network distortion and the resulting chirality enhancement through shrinkage of the network and decrease in pitch. This study demonstrated, for the first time, strong VCD signals of siloxane network forming right-handed versus left-handed twisted and helical

ribbon-like nanostructures. It was demonstrated that the small structural changes due to dehydration upon calcination induces the large enhancement of VCD signals, which reveal that the observed silica chirality originates from a chirally arranged siloxane network expressed from chiral organization of Si—O—Si bonds.

Using such silica nanohelices, we then demonstrated that it is possible to dope inorganic ions such as lanthanide ions directly in the mesoporous silica network of helices without any organic mediates [32]. After the transcription from organic nanohelix to silica helices and washing away the organic template, the obtained silica nanohelices were immersed in terbium(III) acetate aqueous solution (20 mM, 30 ml) for 18 hours and thoroughly washed with water (typically six times washing) until unadsorbed terbium(III) acetate was almost completely removed as checked by the ultraviolet (UV) absorption spectra. The washed hybrids were freeze dried and then calcined at 600–1200 °C for four hours in air (Figure 8.3a). When the calcination temperature ranges between 600 and 1000 °C, Tb^{3+}-doped nanohelices maintained the helical shape. When the calcination temperature reached 1100 °C, the helical shape started to disintegrate while keeping the fibrous structure. No defined structure was observed anymore when the calcination temperature increased up to 1200 °C (Figure 8.3b). Energy dispersive X-ray (EDX) spectroscopy detected signals ascribed to terbium, which showed that the Tb^{3+} concentrations in the nanosilicas calcined at 600–1200 °C were estimated to be around 0.31 at% (2.4 wt%, standard deviation, 0.02 at% and 0.1 wt%).

Figure 8.3c (i) and (ii) show the solid-state excitation and emission spectra, respectively, of L-SiO_2:Tb^{3+} calcined at different temperatures. Emission spectra of L-SiO_2:Tb^{3+} (Figure 8.3c (ii)) showed four sharp emission peaks at 489, 544, 586, and 621 nm, which correspond to the transition from the $^5D_4$ state to the ^7F_J ($J = 6, 5, 4,$ and 3) states of Tb^{3+}, respectively [33–36]. In the excitation spectra of L-SiO_2:Tb^{3+} monitored at 544 nm (Figure 8.3c (i)), excitation bands were observed at around 230 nm (Figure 8.3c) (i), which were attributed to the $4f^8 - 4f^7 5d$ transition of Tb^{3+} [37–39]. The emission intensity increased with increasing calcination temperature up to 900 °C. This is probably due to the decrease in OH groups of nanosilica with increasing calcination temperature and the resulting reinforced interaction of Tb^{3+} with $(Si–O)_n$ [17]. Over 1000 °C, the emission intensity decreased drastically, probably due to the transformation of individually dispersed Tb^{3+} into nanoparticles, as terbium oxide, for which only the Tb atoms in the outer surface can be emissive. We then performed electronic circular dichroism (ECD) spectral measurement using a diffuse reflectance method and circularly polarized luminescence (CPL) spectral measurement of SiO_2:Tb^{3+}. The principal question here was to know if such bare Tb^{3+} ions doped in the amorphous helical siloxane network without any organic mediates "feel" the morphological chirality of the surrounding silica helices. For the calcined SiO_2:Tb^{3+} beyond 600 °C, the clear ECD signals specific to Tb^{3+} ions were observed centered at around 230 nm (Figure 8.3c) (iii)) close to the absorption and excitation $4f^8 - 4f^7 5d$ transition band of Tb^{3+}. The ECD signals slightly decreased with increasing calcination temperature. These results suggest that the chiral coordination of Tb^{3+} with Si–O(H) decreased with the increasing calcination temperature, even though their helical shapes were maintained. When

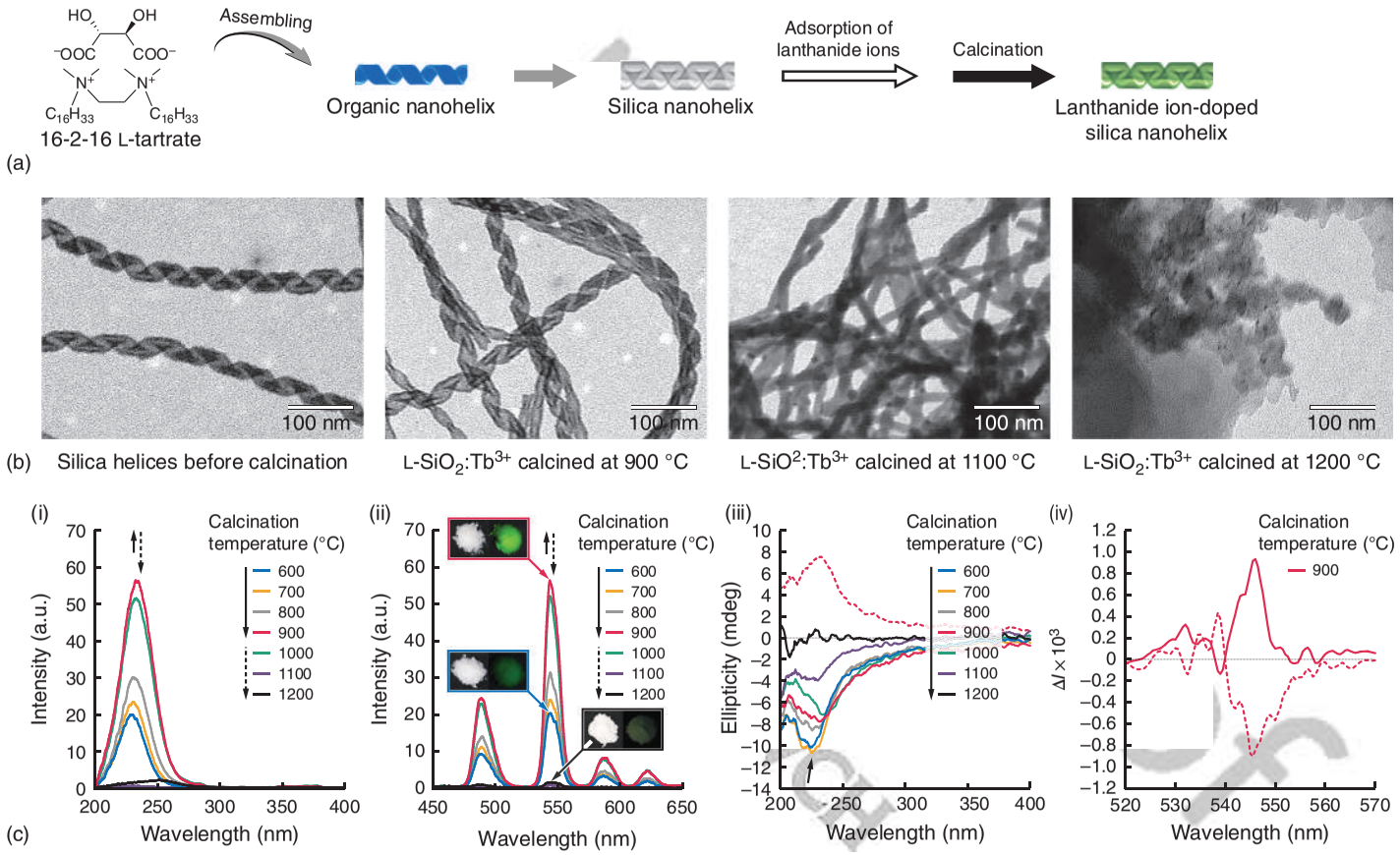

Figure 8.3 (a) Schematic illustration of the preparation procedure of lanthanide ion-doped silica nanohelices. (b) STEM images of silica nanohelices prepared from 16-2-16 L-tartrate without calcination and L-SiO_2:Tb^{3+} calcined at 900, 1100, and 1200 °C. (c) (i) Excitation (emission wavelength 544 nm), (ii) emission (excitation wavelength: 230 nm), (iii) ECD and (iv) CPL spectra of SiO_2:Tb^{3+} calcined at different temperatures (600–1200 °C); measurement temperature: 25 °C. The spectra of L- and D-SiO_2:Tb^{3+} are denoted by solid and dashed lines, respectively. Insets in (ii) show pictures of L-SiO_2:Tb^{3+} calcined at 600, 900, and 1200 °C in daylight (left) and under 254 nm UV light in the dark (right). The CPL spectra were normalized to 1 V of the maximum direct current voltage. Source: Reproduced with permission from Harada [32], Figure 1-3/Royal Society of chemistry

the calcination temperature surpassed 1000 °C, the ellipticity decreased showing a strong correlation between the nanohelical morphology and the ECD signal, which allows us to conclude that the chiral property of Tb^{3+} comes from the helical silica with a chirally arranged siloxane network surrounding Tb^{3+}, although the ensemble of the silica network is amorphous. We suggest that the 4f orbital of Tb^{3+} is chirally distorted by the effect of the interaction of the chirally arranged Si–O to Tb^{3+}. Such inorganic ions entrapped in the silica nanohelices also showed CPL signals as shown in Figure 8.3c (iv). SiO_2:Tb^{3+} calcined at 900 °C, which were mounted in a 0.01 cm path length quartz cell showed the mirror image CPL signals at around 545 nm when irradiated at 230 nm. The dissymmetry factor was estimated to be $|1 \times 10^{-3}|$.

The silica nanohelices immersed in the solution of inorganic ions and then calcined show induced chiroptical properties such as ECD and CPL demonstrating direct chirality induction to inorganic ions (Tb^{3+}). This induction was observed at very low atomic concentration such as 0.3 at% and was still clearly observable. We suggest that the inorganic silica acts as a chiral ligand for Tb^{3+}. This, in turn, shows that the lanthanide ions doped in the silica network can play a role to probe the degree of the chiral order of Si–O–Si network.

8.3 Silica Nanohelices as Platforms to Organize Nonchiral Objects

These inorganic or hybrid nanoobjects with morphologically controlled chirality can be used as templates to induce chirality to achiral functional molecules or nanoparticles. Two approaches were chosen. One is to use the purely silica helices as platforms for grafting molecules or nanoparticles where helices serve as purely morphological support and the other is to use the hybrid organic assemblies–silica, in which case, chiral crystalline organization of gemini surfactants protected by silica wall serve as molecular recognition sites during the ion exchange and chirality induction. In the following, several examples of both the cases are described.

8.3.1 Silica Helices as Platforms for Grafting Molecules

In the first example, chiral induction to small molecules such as pyrene and perylene derivatives is demonstrated when they are covalently grafted onto nanometric silica helices [40, 41] (Figure 8.4). The grafted chromophores are found to exhibit induced chiroptical signals despite the absence of asymmetric atoms. The observed chiral induction is attributed to supramolecular chiral organization of the chromophores on the helical silica surface, as evidenced by the variation of the ICD signal with increasing surface density of the achiral chromophore [40]. The magnitude of the induced chiroptical signals increases exponentially with the grafting density of the chromophores, suggesting that chiral induction occurs cooperatively.

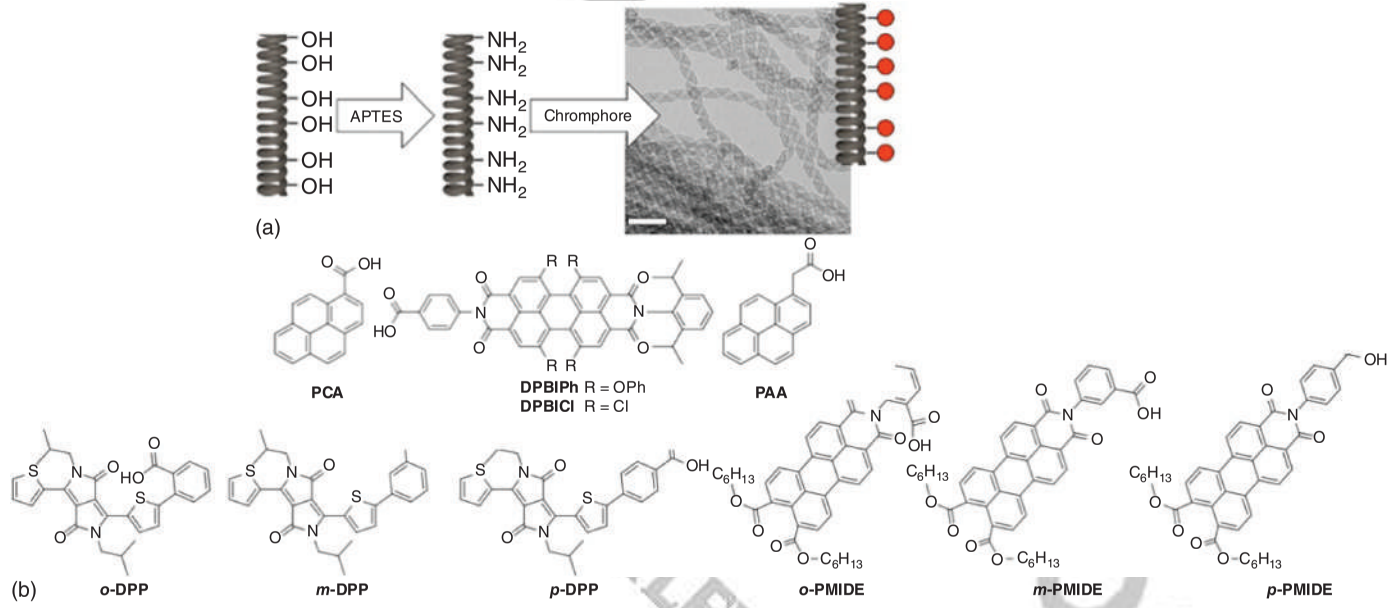

Figure 8.4 (a) Process for the preparation of silica helices covalently grafted with different organic chromophores and TEM image of a sample of helices grafted with 1-pyreneacetic acid (**PAA**, Scale bar: 100 nm). (b) Examples of covalently grafted chromophores on the silica nanohelices. (c) (left) CD and absorbance spectroscopy of **PCA** in ethanol solution (black) and dispersions in ethanol of right- (red) and left-handed (blue) helices grafted by **PCA**. (right) TEM images of the structures (scales bar: 100 nm) and fluorescence spectroscopy of **PCA** solution (black) and right- (red) and left-handed (blue) helices grafted by **PCA**. (d) Absolute value of CD of nanostructures grafted with different density of **PAA** (solid red line: 0.28 nm^{-2}, solid blue line: 0.19 nm^{-2}, dashed red line: 0.13 nm^{-2}, and dashed blue line: 0.06 nm^{-2}). Middle: Absorbance of **PAA** in solution (black) and grafted with different density on the surface of nanostructures (solid red line: 0.28 nm^{-2}, solid blue line: 0.19 nm^{-2}, dashed red line: 0.13 nm^{-2}, dashed blue line: 0.06 nm^{-2}, dotted red line: 0.07 nm^{-2}, and dotted blue line: 0.03 nm^{-2}). Bottom: Evolution of the dissymmetry factor (at 358 nm) with the density of **PAA** on the surface of nanostructures. Inset shows the same data in a semi-log plot with a linear best-fit to $y = ax + b$ with $a = -12.2$ and $b = 16.5$ ($r^2 = 0.982$). Source: Reproduced with permission from American Chemical Society, 2020.

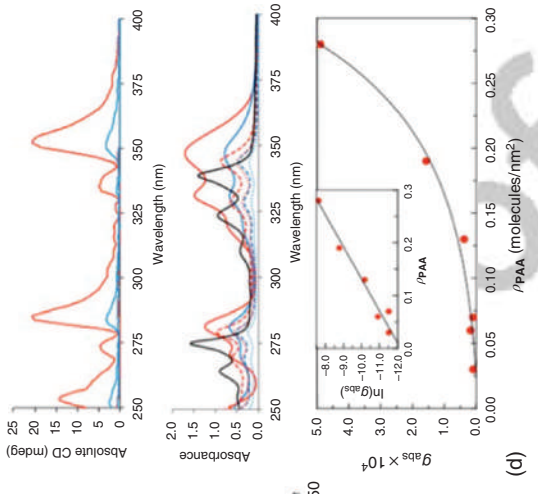

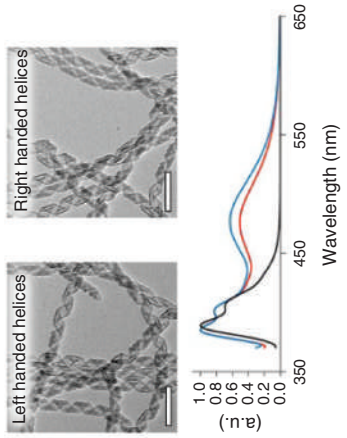

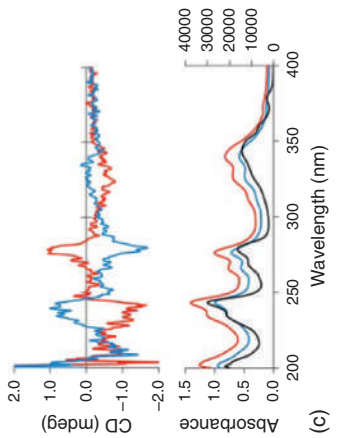

Figure 8.4 (*Continued*)

These results demonstrate the possibility to induce chiroptical properties onto achiral molecular chromophores using inorganic mesoscopic chiral platforms having no chiral molecules, molecular prints, or ligands but purely morphological chirality at tens of nanometers scale (left- or right-handed silica helix).

We have also studied the grafting of diketopyrrolopyrroles and perylenemonoimidodiesters, and the effect of substitution of benzoic acid in the *ortho*, *meta*, and *para* positions were compared (Figure 8.4b) [41]. Again, the chirality at the mesoscopic level induced chiroptical properties to these achiral molecular chromophores. We found that all six achiral benzoic acid-based on DPP and PMIDE cores, (*o*-DPP, *m*-DPP, *p*-DPP, *o*-PMIDE, *m*-PMIDE, and *p*-PMIDE) exhibit excimer emission upon grafting to silica helices. Their grafting density η is directly determined by the point of attachment, with $\eta(para) > \eta(meta) > \eta(ortho)$ for both the DPP and PMIDE series on either ribbons or helices. Although in general excimer emission is expected to be dependent on grafting density (as in the DPP series), the contrary is true for the PMIDE series. Here, the *o*-PMIDE derivative with the lowest grafting density shows the highest excimer contribution. This can be rationalized on the basis of the propensity for the perylene chromophore to form excimers, given sufficient conformational mobility. The higher grafting densities of the *m* and *p*-PMIDE derivatives may result in less conformational freedom leading to lower excimer formation yields from the localized excited state. For both the series of chromophores, the results indicate that the density of chromophores on the surface of the silica nanostructures is directly correlated with the value of g_{abs}. The lowest values of grafting density were obtained for the derivatives substituted in the *ortho*-position, resulting in low g_{abs} values.

The grafted structures are weakly (diketopyrrolopyrroles) or strongly (perylenemonoimidodiesters) emissive, exhibiting both locally excited state emission and a broad, structureless emission assigned to excimers. The dissymmetry factors obtained using CD highlight optimized supramolecular organization between the chromophores for enhancing the chiroptical properties of the system. In the *ortho*-derivatives, poor organization due to steric hindrance is reflected in a low density of chromophores on walls of the silica-nanostructures (<0.1 vs. >0.3 and up to 0.6 molecules/nm^2 for the *ortho* and *meta* or *para* derivatives, respectively) and lower g_{abs} values than in the other derivatives ($g_{abs} < 2\times10^{-5}$ vs. 6×10^{-5} for the *ortho* and *para* derivatives, respectively). The *para* derivatives presented a better organization and increased values of g_{abs}. The lowest values of grafting density were obtained for the derivatives substituted in the *ortho*-position, resulting in low g_{abs} values. From previous results, we conclude that insomuch as excimer emission can be related to surface density, it provides an indirect correlation to the induced chiroptical properties. However, this relationship is tenuous since systems in which conformational motion is needed to favor excimer formation (e.g. bulky chromophores) will show the reverse relationship. This is the case for the PMIDE series in which chiroptical induction and excimer emission intensity are negatively correlated.

Such silica templates provide highly robust and versatile chiral nanostructures with good tolerance toward variations in temperature and solvent. Not only the size and pitch but also the handedness of the silica helices can be tailored as needed,

making them good potential candidates for the design of robust and tunable chiral surfaces on which achiral dyes can be assembled to obtain chiroptical materials. The correlation between the observed dissymmetry factor and the grafted molecular density suggests that the difference in scale between molecules and nanometric objects is such that individual surface-bound dye molecules grafted on the much larger silica surface do not exhibit chiroptical properties. However, upon forming surface-bound supramolecular aggregates, chiroptical properties are observed due to chiral induction from the template. Such assembly-induced chirality induction from the surface of chiral templates may be quite general.

8.3.2 Silica Helices as Platforms for Grafting Nanoparticles

These nanometric silica helices are also used as chiral templates in order to organize GNPs to prepare a collection of helical GNPs superstructures (called Gold helices hereafter). These nanoobjects exhibit well-defined arrangement of GNPs (with diameters varying between 4 and 10 nm) following the helicity of the silica template. Strong chiroptical activity is evidenced by ECD spectroscopy at the wavelength of the surface plasmon resonance (SPR) of the GNPs with a dissymmetry factor (*g*-factor) of the order of 10^{-4} [8, 9]. Our study clearly showed that these optical activities depend both on the size and the organization of the GNPs on the surface of the helical silica template that are closely correlated with the surface chemistry of both the GNPs and the silica helices (Figure 8.5). The CD signals of these GNP systems were simulated according to coupled-dipole method (CDM), and the effect of particles' size, disorder, grafting density, and the polydispersity were evaluated. The simulations qualitatively reproduced very well the observed CD signals in terms of the spectra shape. The g-factor of these systems increased with the GNP size. However, the simulated g-factor is 1–2 orders of magnitude higher than the experimental value. This discrepancy is likely due to the GNP disorder, the variation in the GNP density, the polydispersity of GNPs, and silica helices. The simulations based on the positions of GNPs estimated by TEM led to the g-factor close to the measured one Figure 8.5d).

AQ3

This approach was expanded to other nanoparticles such as quantum dots [42, 43]. Indeed these nanoparticles are perfect candidates to design chiroptical nanoobjects, as they both exhibit excellent absorption and luminescent properties. Perovskite $CsPbBr_3$ nanocrystals (PNCs) are grafted on the surface of silica nanohelices by a ligand exchange method. Grazing incidence X-ray scattering, tomography and cryoelectron microscopy (EM) have shown closely and helically packed PNCs on the silica helices, PNCs are much more closely organized on dried helices than in suspension (Figure 8.6). Interestingly, they do not show any detectable chiroptical properties when suspended in solvent, suggesting that ligands collapse and a higher interaction occurs between the both when dried, which may induce higher self-organization with a three-dimensional spiral arrangement of the PNCs along with the inorganic chiral silica nanohelices. In contrast, in a dried film state, they show large CD and CPL signals with dissymmetric factor up to 6×10^{-3} (Figure 8.6b) Simulations based on the CDM demonstrate that the CD comes from the dipolar

Color Fig: **8.5**

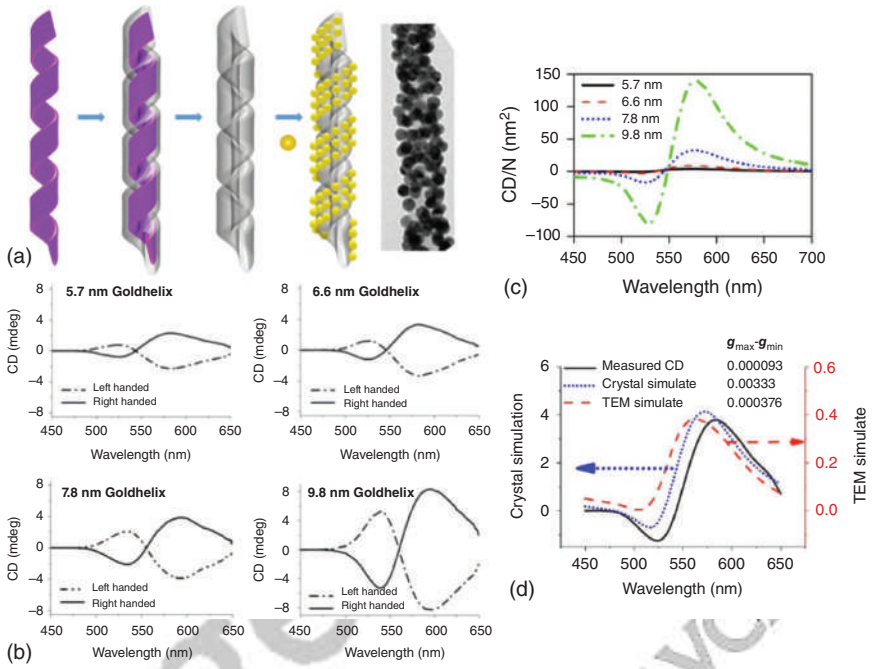

Figure 8.5 Silica nanohelices synthesized from sol–gel condensation of TEOS on self-assembled organic nanostructures are used as a matrix to prepare helical GNPs superstructures (Gold helix) with tunable and well-defined handedness. (a) Scheme of fabrication of GNPs@ SiO_2 helix. (b) Corresponding electronic CD spectra of the Gold helices for four different diameters. Dashed lines represent left-handed Gold helix, and solid lines represent right-handed Gold helix. (c) Influence of the GNP radius on the CD/N spectra simulated by considering perfectly aligned (crystalline organization) and monodisperse GNPs forming right-handed helical organization. (d) Measured CD signal obtained for 5.7 nm GNPs (black solid line) is compared with the simulated CD signal obtained for perfect crystalline organization ($\sigma = 0$, blue dotted line) as well as the CD signal simulated for the real position of the GNPs (3D tomography, red dashed line). Source: Reproduced with permission from American Chemical Society, 2018.

interaction between PNC assembled into a chiral structure (Figure 8.6c,d). For the adjacent particles to "feel" the chirality, the interparticle distances need to be very close to each other with good alignment, which is likely why solvated samples with larger particle distances with much less ordered organization do not show any detectable CD. These films show an excellent photostability in their absorbance and CD properties; however, they strongly lose their emissivity upon heating up to 80 °C.

8.3.3 Coassembly of Chiral Self-assembly and Achiral Dyes

Another method to induce chirality to achiral entities is to use the hybrid organic assemblies-silica. In the first example, we demonstrated ICD from monoatomic anions such as fluoride, bromide, and iodide. This was detected using helically

Color Fig: **8.6**

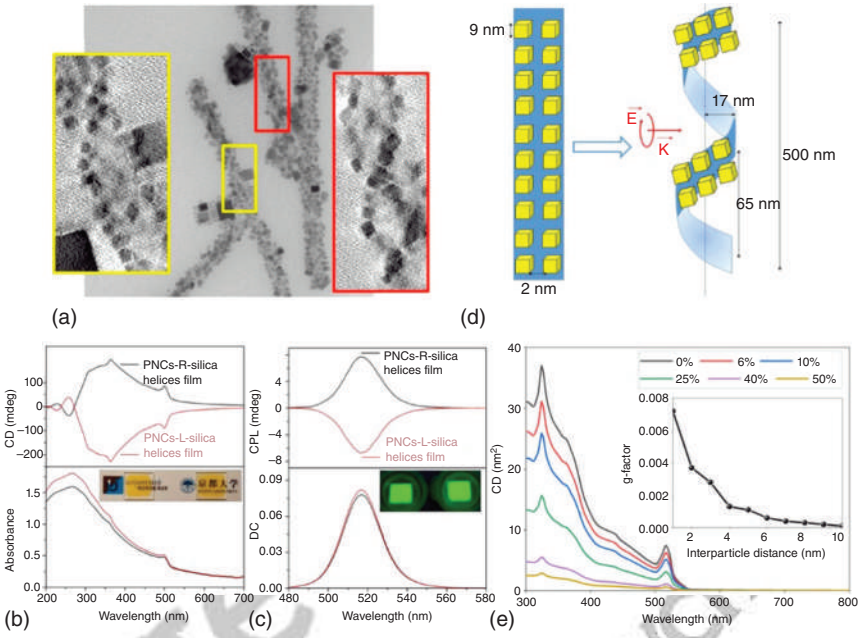

Figure 8.6 (a) TEM image of nanohelices@PNCs and the cross-sections obtained with the tomography 3D reconstructions (framed in red and yellow) for dried film. (b) Absorbance and CD spectra and (c) DC and CPL spectra of PNCs-right handed-silica nanohelices (black) and PNCs-left handed-silica nanohelices film (red) dried at 4 °C. The inset picture in (b) shows the drop-cast film from right-handed and left-handed samples under natural light. The inset picture in (c) shows the drop-cast films from right-handed and left-handed samples irradiated under a UV lamp at 365 nm. The mean values of data measured at 0° and 90° are shown in order to eliminate the contribution of linear dichroism. The dissymmetric factors for PNCs-L/R-silica helices are g_{abs} ($_{abs}$ 367.5 nm) ~6.2×10^{-3}/−6.4×10^{-3} and g_{lum} ($_{em}$ 517.5 nm) ~6.9×10^{-3}/−5.7×10^{-3}. (The names, emblems, and logotypes as shown here credit to University of Bordeaux and Kyoto University, respectively.). (d) Schematic representation of helically ordered PNCs. All simulations are performed by considering a NPCs size of 9 nm. Two rows of PNCs are perfectly aligned around the helix; the radius of the helix is 34 nm and the pitch is 65 nm (e) Simulated CD of a PNC-silica helix for several amount of randomly removed NPCs. In inset of (e), the evolution of the g-factor at a 516 nm wavelength with the interparticle distance (1–10 nm) is simulated by removing 30% of NPCs (which gives the g-factor as observed experimentally in dried sample). Source: Reproduced with permission from American Chemical Society, 2020.

arranged molecular assemblies of nonchiral cationic gemini surfactants [16-2-16] stabilized with silica coating. Helical and twisted ribbons of gemini (16-2-16 tartrate) surfactant–silica composites were prepared; then tartrate anions in the composites are replaced by achiral anions (Figure 8.7 top). ICD signal was observed for the monoatomic anions, which originates from their coassembly with memorized chiral organization of 16-2-16 surfactants.

This approach was further extended for other molecular anions, and we have demonstrated the generality of this methodology to induce chiroptical properties to a large range of anions. Indeed, when the 16-2-16 Cl_2-silica composite dispersions

Color Fig: **8.7**

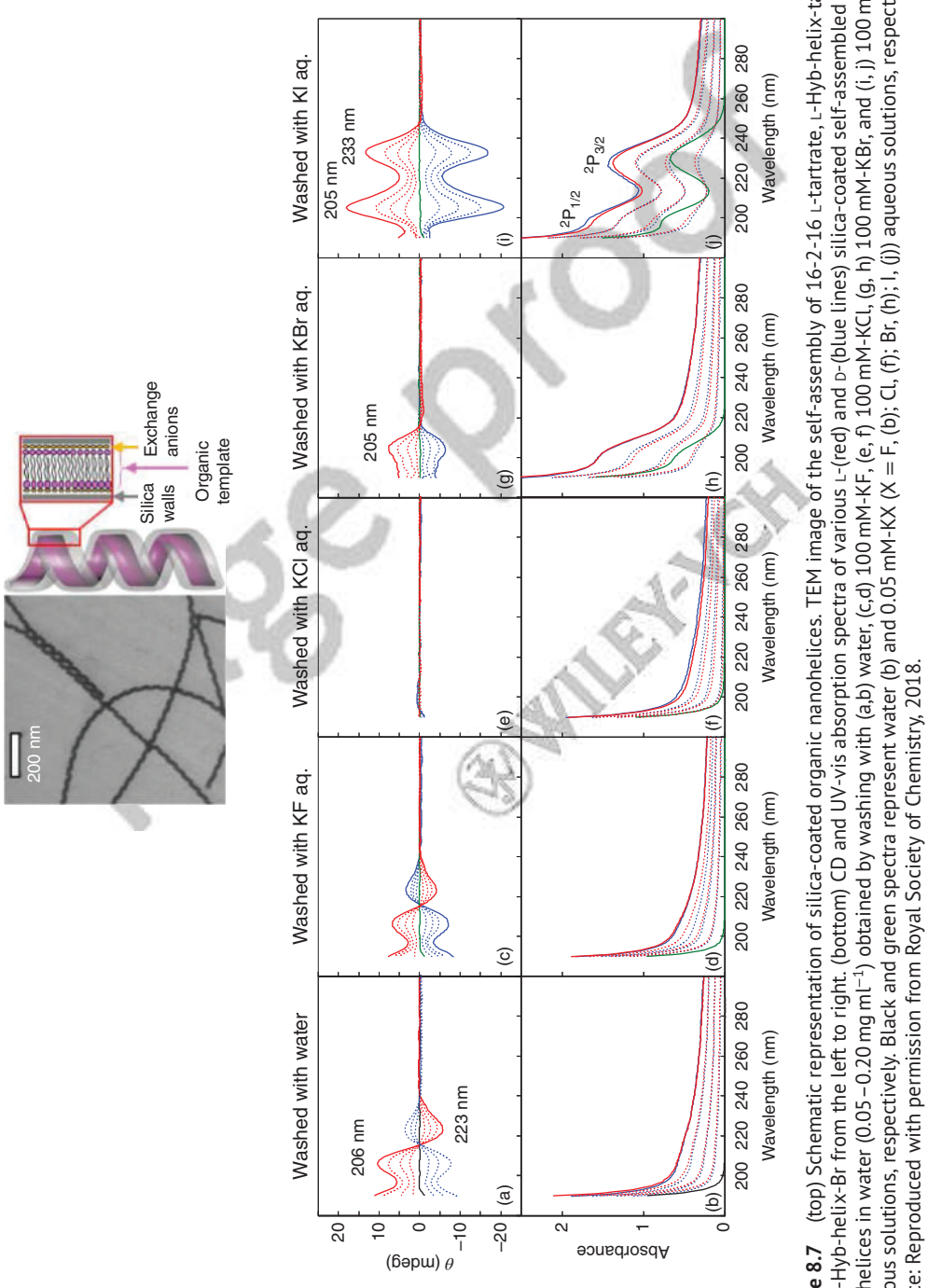

Figure 8.7 (top) Schematic representation of silica-coated organic nanohelices. TEM image of the self-assembly of 16-2-16 L-tartrate, L-Hyb-helix-tart, and L-Hyb-helix-Br from the left to right. (bottom) CD and UV-vis absorption spectra of various L-(red) and D-(blue lines) silica-coated self-assembled nanohelices in water (0.05–0.20 mg ml^{-1}) obtained by washing with (a,b) water, (c,d) 100 mM-KF, (e, f) 100 mM-KCl, (g, h) 100 mM-KBr, and (i, j) 100 mM-KI aqueous solutions, respectively. Black and green spectra represent water (b) and 0.05 mM-KX (X = F, (b); Cl, (f); Br, (h); I, (j)) aqueous solutions, respectively. Source: Reproduced with permission from Royal Society of Chemistry, 2018.

Self-assembling molecule: Cationic gemini surfactant with chiral counterion

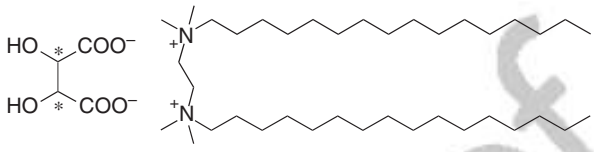

16-2-16 tartrate

Achiral anionic guests (1): Inorganic molecular anions

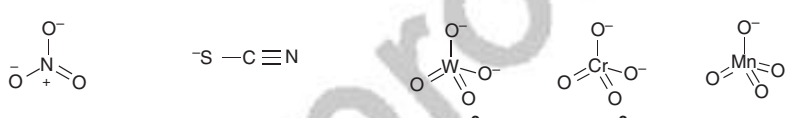

NO_3^- **SCN^-** **WO_4^{2-}** **CrO_4^{2-}** **MnO_4^-**

Achiral anionic guests (2): Anionic polyaromatic chromophores

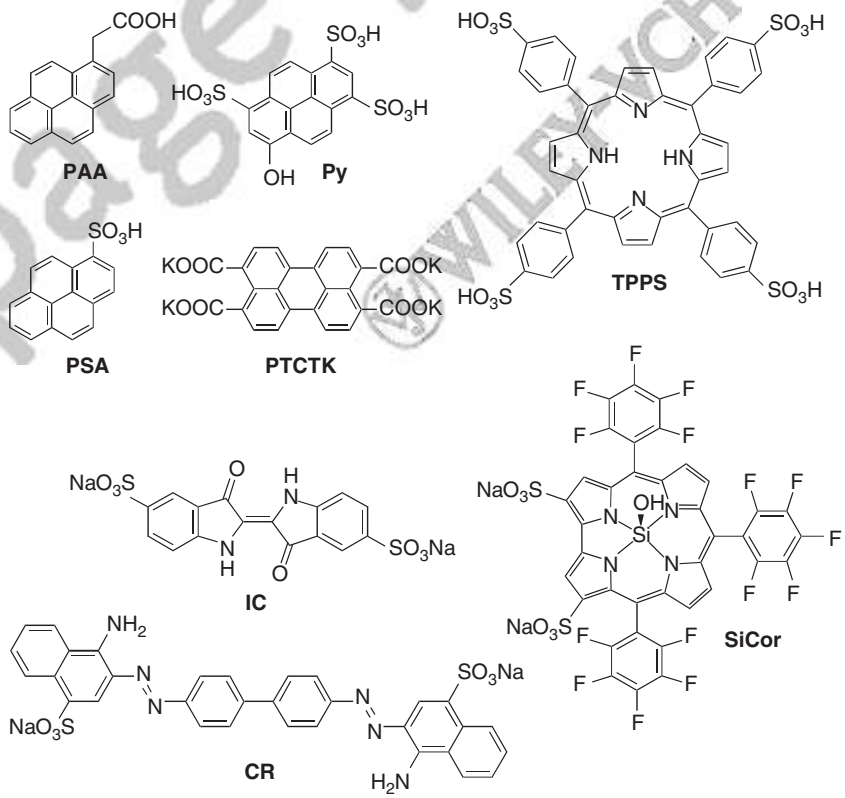

PAA **Py** **TPPS** **PSA** **PTCTK** **IC** **SiCor** **CR**

Figure 8.8 Molecular structures of achiral inorganic or polyaromatic anions. Source: Reproduced with permission from Chirality. 2021;33:494–505 " / John Wiley & Sons.

Color Fig: **8.9**

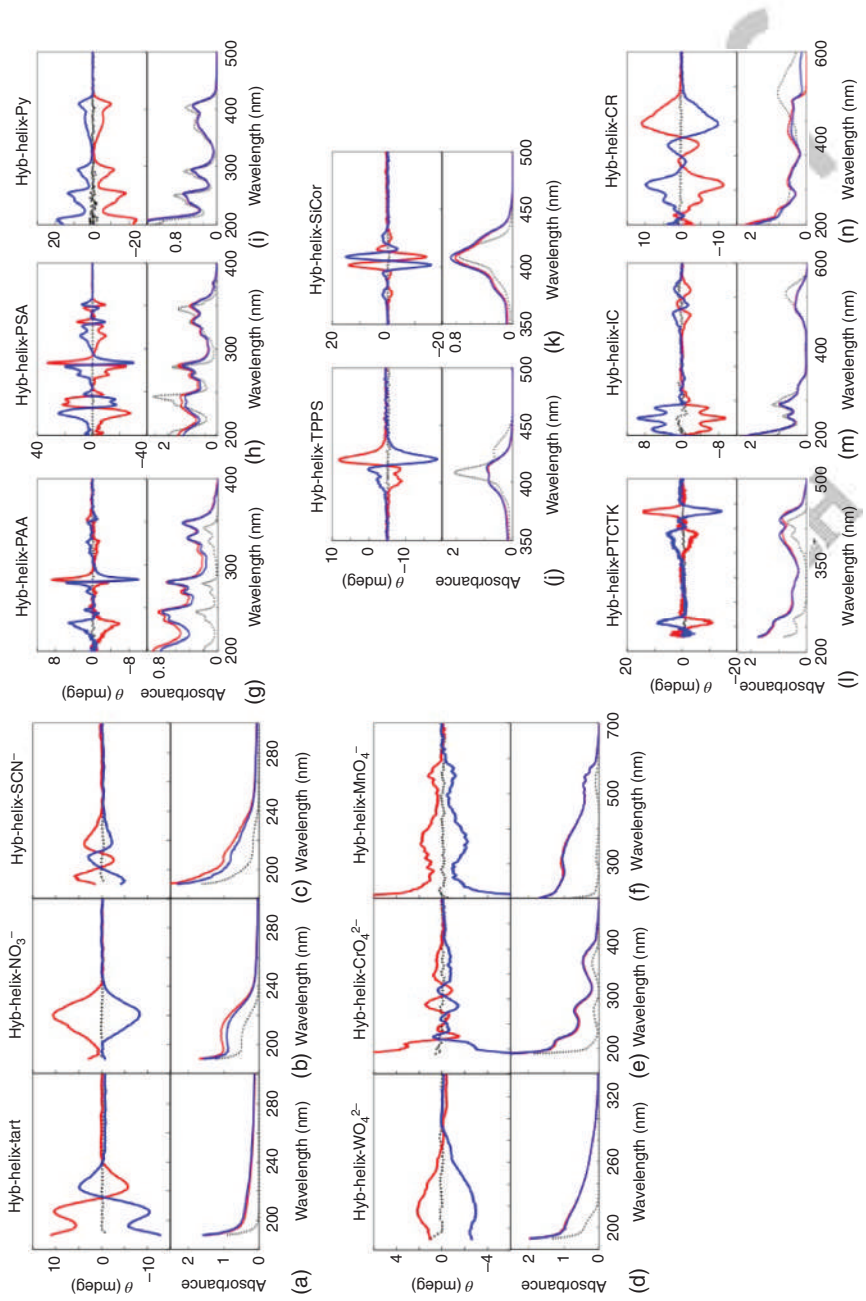

Figure 8.9 CD (top) and UV-vis absorption (bottom) spectra of RH- (red lines) and LH- (blue lines) Hyb-helix (gemini-tartrate) (0.20 mg ml^{-1} in water) after washing with (a) water, (b) KNO_3 aq., (c) KSCN aq., (d) Na_2WO4 aq., (e) K_2CrO_4 aq., (f) $KMnO_4$ aq. (g) PAA aq., (h) PSA aq., (i) Py aq., (j) TPPS aq., (k) SiCor aq., (l) PTCTK aq., (m) IC aq., and (n) CR aq. without (black dotted lines) and with RH- (red lines) and LH- (blue lines), Hyb-helices, respectively. All samples were measured at 20 °C. Source: Reproduced with permission from Scalabre et al. [44]/John Wiley & Sons.

Color Fig: **8.10**

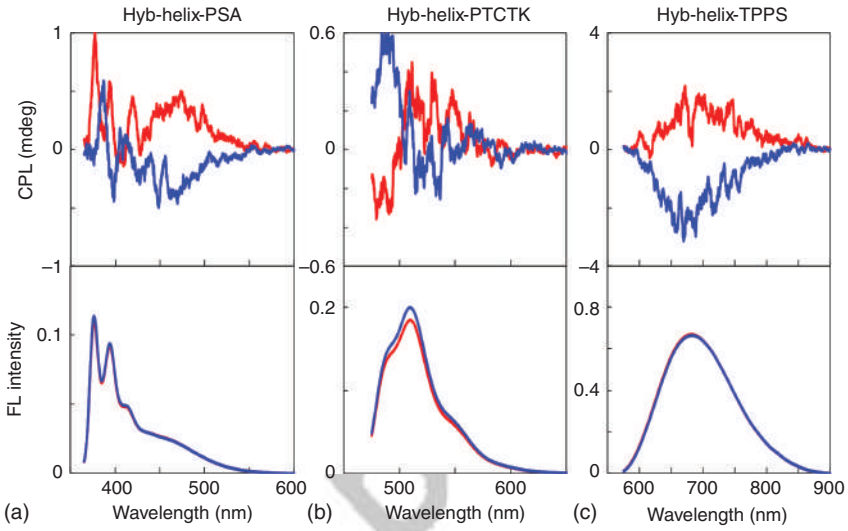

Figure 8.10 CPL and fluorescence spectra of (a) PSA (ex 340 nm), (b) PTCTK (ex 430 nm), and (c) TPPS (ex 410 nm) in the presence of RH- (red line) or LH- (blue line) handed hybrid helices. Source: Reproduced with permission from Scalabre et al. [44]/John Wiley & Sons.

were mixed with the aqueous solution of various achiral molecular anions, the ion exchange between the chloride and other anions occurred on most of the time, and we have clearly demonstrated the emergence of chiroptical properties from the latter. These anions include [1] inorganic molecular anions with different shapes such as trigonal planar nitrate (NO_3^-), linear thiocyanate (SCN^-), tetrahedral orthotungstate(VI) (WO_4^{2-}), chromate(VI) (CrO_4^{2-}), and permanganate(VII) (MnO_4^-); and [2] anionic polyaromatic chromophores such as biphenyle, pyrene, perylene, and porphyrin derivatives [44] (Figures 8.8 and 8.9).

For luminescent anions, we could observed ICPL from the confined achiral anionic fluorophores, in particular for pyrene sulfonic acid; the ICPL was observed from intermolecular excimer through excimer formation, which is a rare observation to date for achiral molecules (Figure 8.10).

These results indicate that nonchiral cationic surfactant gemini paired with chiral counterion, tartrate that forms helical self-assembly can keep their chiral assembly with chiral arrangement when it is confined inside helical silica nanomatrices even after the tartrate is exchanged by other achiral anions, inducing chiroptical properties to these anions.

8.4 Conclusion

This chapter shows how helical nanosilica platform can be used to create chiral environment at nano-scale, and induce chiroptical signals from a large range of achiral molecules and nanoparticles.

Color Fig: **8.11**

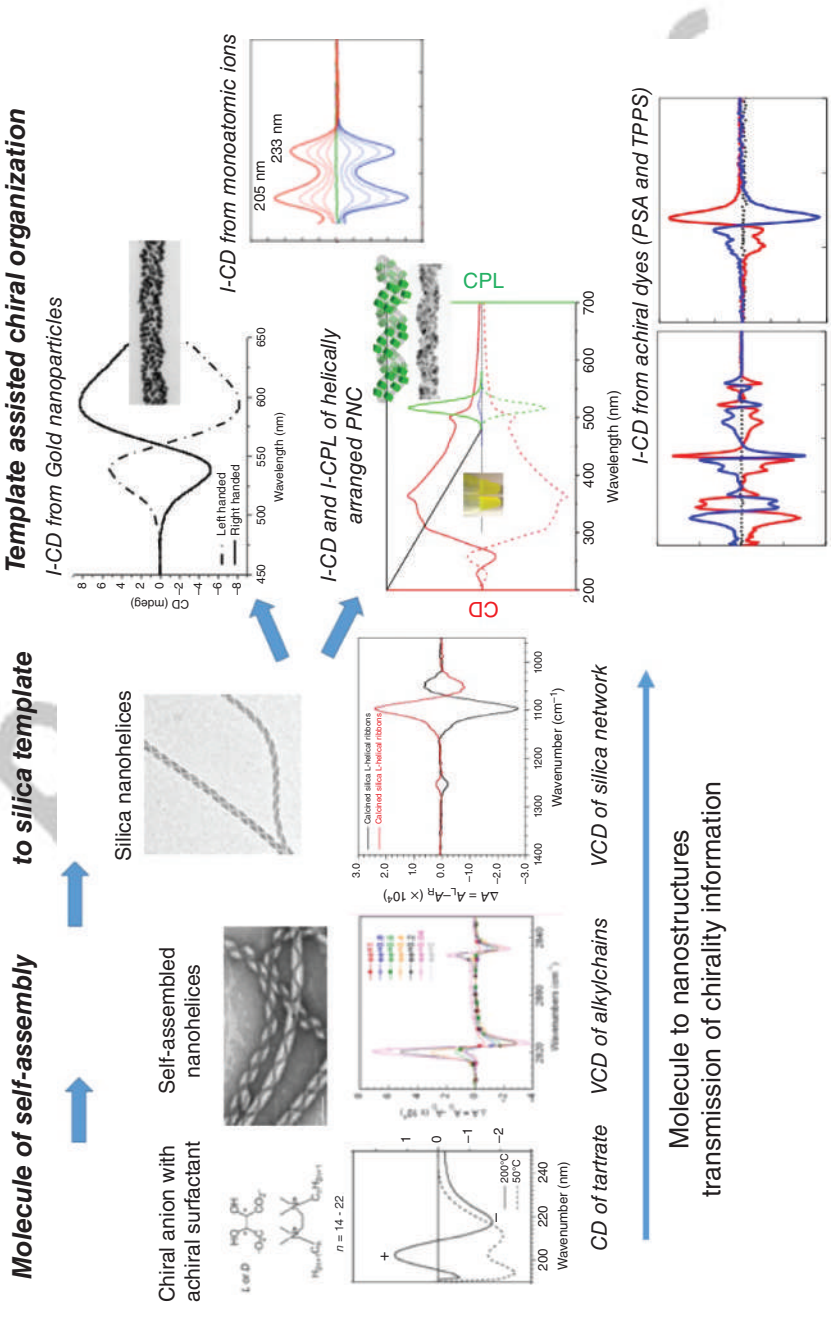

Figure 8.11 Multistep transmission of chirality information from tartrate anions to gemini surfactant, to silica nanohelices, then to chromophores, nanoparticles, or monoatomic ions. The only chiral component is the original tartrate.

First, the chirality of a dianionic molecule (L- or D-tartrate) ion paired with achiral dicationic *n*-2-*n* gemini surfactant self-organize together into right- or left-handed chiral nanostructures. The chiral arrangement both of tartrate and *n*-2-*n* molecules were clearly evidenced by VCD and XRD. These chiral molecular assemblies with controllable chirality were used to synthesize chiral inorganic or hybrid nanohelices, which were then used as the template to induce chirality in achiral functional molecules, nanoparticles, or monoatomic ions. Two approaches were presented. In the first one, the surfaces of these silica nanohelices were functionalized for the grafting of achiral dyes or nanoparticles, leading to their chiral organization evidenced by ECD and CPL signals. In the second method, various types of achiral anions are used to replace the original tartrate anions confined in the chiral silica matrices along with gemini surfactant. These anions are then co-organized forming chiral assembly, and, again, chiroptical signals are observed.

The silica helices@chromophores systems presented in this chapter are much more robust than previously reported organic-based chiroptical nanostructures. And the unprecedented multistep transfer mechanism of chiral information from molecules to molecular assemblies, from organic to inorganic templates, then to other achiral molecules, particles, or monoatomic ions (as summarized in the scheme Figure 8.11) is a very interesting example of how to achieve finely controllable chirality from versatile ensembles of emissive entities. Therefore, our approach can lead to very promising applications in the field of light management such as circular polarizers, chiral metamaterials or chiral sensing, 3D displays, and more globally for the data storage, the security, and the communication in the visible range.

References

1 Greenfield, J.L., Wade, J., Brandt, J.R. et al. (2021). Pathways to increase the dissymmetry in the interaction of chiral light and chiral molecules. *Chem. Sci.* 12 (25): 8589–8602.

2 Goto, T., Okazaki, Y., Ueki, M. et al. (2017). Induction of strong and tunable circularly polarized luminescence of nonchiral, nonmetal, low-molecular-weight fluorophores using chiral nanotemplates. *Angew. Chem. Int. Ed. Engl.* 56 (11): 2989–2993.

3 Yoshida, S., Morikawa, S., Ueda, K. et al. (2020). Photoinvertible chiral liquid crystal that affords helicity-controlled aromatic conjugated polymers. *Adv. Opt. Mater.* 8 (20): 2000936.

4 Yan, B., Matsushita, S., and Akagi, K. (2016). An advanced method for preparation of helical carbon and graphitic films using a carbonization substrate. *Chem. Mater.* 28 (23): 8781–8791.

5 Yamamoto, H., Inagaki, T., Park, J. et al. (2021). Helical network polymers embodying high dissymmetry factors in circularly polarized luminescence: photocrosslinking polymerization of acrylate derivatives in chiral smectic liquid crystals. *Macromolecules* 54 (19): 8977–8986.

6 Negrín-Montecelo, Y., Movsesyan, A., Gao, J. et al. (2022). Chiral generation of hot carriers for polarization-sensitive plasmonic photocatalysis. *J. Am. Chem. Soc.* 144 (4): 1663–1671.

7 Gérard, V.A., Gun'ko, Y.K., Defrancq, E., and Govorov, A.O. (2011). Plasmon-induced CD response of oligonucleotide-conjugated metal nanoparticles. *Chem. Commun.* 47 (26): 7383–7385.

8 Gao, J., Wu, W., Lemaire, V. et al. (2020). Tuning the chiroptical properties of elongated nano-objects via hierarchical organization. *ACS Nano* 14 (4): 4111–4121.

9 Cheng, J., Le Saux, G., Gao, J. et al. (2017). GoldHelix: gold nanoparticles forming 3D helical superstructures with controlled morphology and strong chiroptical property. *ACS Nano* 11 (4): 3806–3818.

10 Chen, W., Bian, A., Agarwal, A. et al. (2009). Nanoparticle superstructures made by polymerase chain reaction: collective interactions of nanoparticles and a new principle for chiral materials. *Nano Lett.* 9 (5): 2153–2159.

11 Auguié, B., Alonso-Gómez, J.L., Guerrero-Martínez, A., and Liz-Marzán, L.M. (2011). Fingers crossed: optical activity of a chiral dimer of plasmonic nanorods. *J. Phys. Chem. Lett.* 2 (8): 846–851.

12 Kang, Y.-J., Oh, J.-W., Kim, Y.-R. et al. (2010). Chiral gold nanoparticle-based electrochemical sensor for enantioselective recognition of 3,4-dihydroxyphenylalanine. *Chem. Commun.* 46 (31): 5665–5667.

13 Park, K.H., Noh, T.H., Shim, Y.-B., and Jung, O.-S. (2013). Construction of right-handed-, left-handed-, and racemic helical coordination polymers. Enantioselective recognition using chiral helical crystals. *Chem. Commun.* 49 (38): 4000–4002.

14 Xing, T., Qian, Q., Ye, H. et al. (2022). Gold nanoparticles with helical surface structure transformed from chiral molecules for SERS-active substrates preparation. *Biosens. Bioelectron.* 212: 114430.

15 Xu, L., Wang, X., Wang, W. et al. (2022). Enantiomer-dependent immunological response to chiral nanoparticles. *Nature* 601 (7893): 366–373.

16 Kumar, J., Eraña, H., López-Martínez, E. et al. (2018). Detection of amyloid fibrils in Parkinson's disease using plasmonic chirality. *Proc. Natl. Acad. Sci. U.S.A* 115 (13): 3225–3230.

17 Zhang, Q.-P., Wang, Z., Zhang, Z.-W. et al. (2021). Triptycene-based chiral porous polyimides for enantioselective membrane separation. *Angew. Chem. Int. Ed.* 60 (23): 12781–12785.

18 Yang, Y., Zhang, Y., and Wei, Z. (2013). Supramolecular helices: chirality transfer from conjugated molecules to structures. *Adv. Mater.* 25 (42): 6039–6049.

19 Crassous, J. (2012). Transfer of chirality from ligands to metal centers: recent examples. *Chem. Commun.* 48 (78): 9687–9695.

20 Oda, R., Huc, I., and Candau, S.J. (1998). Gemini surfactants as new, low molecular weight gelators of organic solvents and water. *Angew. Chem. Int. Ed.* 37 (19): 2689–2691.

21 Oda, R., Huc, I., Schmutz, M. et al. (1999). Tuning bilayer twist using chiral counterions. *Nature* 399 (6736): 566–569.

22 Brizard, A., Aime, C., Labrot, T. et al. (2007). Counterion, temperature, and time modulation of nanometric chiral ribbons from gemini-tartrate amphiphiles. *J. Am. Chem. Soc.* 129 (12): 3754–3762.

23 Oda, R., Artzner, F., Laguerre, M., and Huc, I. (2008). Molecular structure of self-assembled chiral nanoribbons and nanotubules revealed in the hydrated state. *J. Am. Chem. Soc.* 130 (44): 14705–14712.

24 Brizard, A., Berthier, D., Aime, C. et al. (2009). Molecular and supramolecular chirality in gemini-tartrate amphiphiles studied by electronic and vibrational circular dichroisms. *Chirality* 21 (1E): E153–E162.

25 Gao, J., Okazaki, Y., Pouget, E. et al. (2021). Slow kinetic evolution of nanohelices based on gemini surfactant self-assemblies with various enantiomeric excess; chiral segregation towards a racemic mixture. *Mater. Chem. Front.* 5 (7): 3021–3028.

26 Sugiyasu, K., Tamaru, S., Takeuchi, M. et al. (2002). Double helical silica fibrils by sol-gel transcription of chiral aggregates of gemini surfactants. *Chem. Commun.* 11: 1212–1213.

27 Delclos, T., Aime, C., Pouget, E. et al. (2008). Individualized silica nanohelices and nanotubes: Tuning inorganic nanostructures using lipidic self-assemblies. *Nano Lett.* 8 (7): 1929–1935.

28 Okazaki, Y., Buffeteau, T., Siurdyban, E. et al. (2016). Direct observation of siloxane chirality on twisted and helical nanometric amorphous silica. *Nano Lett.* 16 (10): 6411–6415.

29 Liu, P., Battie, Y., Okazaki, Y. et al. (2021). Chiral optical scattering from helical and twisted silica nanoribbons. *Chem. Commun.* 57 (90): 12024–12027.

30 Kaneko, Y. and Iyi, N. (2009). Sol–gel synthesis of ladder polysilsesquioxanes forming chiral conformations and hexagonal stacking structures. *J. Mater. Chem.* 19 (38): 7106–7111.

31 Guo, Z., Du, Y., Chen, Y. et al. (2010). Understanding the mechanism of chirality transfer in the formation of a chiral MCM-41 mesoporous silica. *J. Phys. Chem. C* 114 (34): 14353–14361.

32 Harada, T., Yanagita, H., Ryu, N. et al. (2021). Lanthanide ion-doped silica nanohelix: a helical inorganic network acts as a chiral source for metal ions. *Chem. Commun.* 57 (36): 4392–4395.

33 Lin, H., Pun, E.Y.-B., Wang, X., and Liu, X. (2005). Intense visible fluorescence and energy transfer in Dy^{3+}, Tb^{3+}, Sm^{3+} and Eu^{3+} doped rare-earth borate glasses. *J. Alloys Compd.* 390 (1): 197–201.

34 Yang, M., Liang, Y., Gui, Q. et al. (2015). Multifunctional luminescent nanomaterials from $NaLa(MoO_4)_2$:Eu^{3+}/Tb^{3+} with tunable decay lifetimes, emission colors and enhanced cell viability. *Sci. Rep.* 5 (1): 11844.

35 Jia, Z. and Xia, M. (2016). Blue-green tunable color of Ce^{3+}/Tb^{3+} coactivated $NaBa_3La_3Si_6O_{20}$ phosphor via energy transfer. *Sci. Rep.* 6 (1): 33283.

36 Kataoka, T., Shiba, K., Wang, L.Y. et al. (2017). Hybrid preparation of terbium(iii)-doped mesoporous silica particles with calcium phosphates. *RSC Adv.* 7 (32): 19479–19485.

37 Reisfeld, R. (1972). Inorganic ions in glasses and polycrystalline pellets as fluorescence standard reference materials. *J. Res. Natl. Bur. Stand.* 76 (6): 613.

38 Guodong, Q., Minquan, W., Mang, W. et al. (1997). Structural evolution and fluorescence properties of Tb^{3+}-doped silica xerogels in the gel to glass conversion. *J. Lumin.* 75 (1): 63–69.

39 Kang, X., Huang, S., Yang, P. et al. (2011). Preparation of luminescent and mesoporous Eu^{3+}/Tb^{3+} doped calcium silicate microspheres as drug carriers via a template route. *Dalton Trans.* 40 (9): 1873–1879.

40 Scalabre, A., Gutierrez-Vilchez, A.M., Sastre-Santos, A. et al. (2020). Supramolecular induction of topological chirality from nanoscale helical silica scaffolds to achiral molecular chromophores. *J. Phys. Chem. C* 124 (43): 23839–23843.

41 Álvaro-Martins, M.J., Garcés-Garcés, J., Scalabre, A. et al. (2022). Disentangling excimer emission from chiral induction in nanoscale helical silica scaffolds bearing achiral chromophores. *ChemPhysChem* e202200573.

42 Liu, P., Chen, W., Okazaki, Y. et al. (2020). Optically active perovskite $CsPbBr_3$ nanocrystals helically arranged on inorganic silica nanohelices. *Nano Lett.* 20 (12): 8453–8460.

43 Liu, P., Battie, Y., Decossas, M. et al. (2021). Chirality induction to CdSe nanocrystals self-organized on silica nanohelices: tuning chiroptical properties. *ACS Nano* 15 (10): 16411–16421.

44 Scalabre, A., Okazaki, Y., Kuppan, B. et al. (2021). Chirality induction to achiral molecules by silica-coated chiral molecular assemblies. *Chirality* 33 (9): 494–505.